Supplementary Information for

Buckling and twisting of advanced materials into morphable 3D mesostructures

Hangbo Zhao[a,1], Kan Li[b,c,d,1], Mengdi Han[a], Feng Zhu[b,c,d,e], Abraham Vázquez-Guardado[f,g], Peijun Guo[h], Zhaoqian Xie[b,c,d,i], Yoonseok Park[a], Lin Chen[j], Xueju Wang[a,k], Haiwen Luan[b,c,d], Yiyuan Yang[c], Heling Wang[b,c,d], Cunman Liang[a,l,m], Yeguang Xue[b,c,d], Richard D. Schaller[h,n], Debashis Chanda[f,g,o], Yonggang Huang[a,b,c,d,2], Yihui Zhang[p,q,2], and John A. Rogers[a,c,d,n,r,s,t,u,v,2]

[a]Center for Bio-Integrated Electronics, Northwestern University, Evanston, IL 60208; [b]Department of Civil and Environmental Engineering, Northwestern University, Evanston, IL 60208; [c]Department of Mechanical Engineering, Northwestern University, Evanston, IL 60208; [d]Department of Materials Science and Engineering, Northwestern University, Evanston, IL 60208; [e]School of Logistics Engineering, Wuhan University of Technology, 430063 Wuhan, China; [f]NanoScience Technology Center, University of Central Florida, Orlando, FL 32826; [g]CREOL, The College of Optics and Photonics, University of Central Florida, Orlando, FL 32816; [h]Center for Nanoscale Materials, Argonne National Laboratory, Lemont, IL 60439 ; [i]Department of Engineering Mechanics, Dalian University of Technology, 116024 Dalian, China; [j]State Key Laboratory for Mechanical Behavior of Materials, School of Materials Science and Engineering, Xi'an Jiaotong University, 710049 Xi'an, China; [k]Department of Mechanical and Aerospace Engineering, University of Missouri-Columbia, Columbia, MO 65211; [l]Key Laboratory of Mechanism Theory and Equipment Design of Ministry of Education, Tianjin University, 300072 Tianjin, China; [m]School of Mechanical Engineering, Tianjin University, 300072 Tianjin, China; [n]Department of Chemistry, Northwestern University, Evanston, IL 60208; [o]Department of Physics, University of Central Florida, Orlando, FL 32816; [p]Center for Flexible Electronics Technology, Tsinghua University, 100084 Beijing, China; [q]Applied Mechanics Laboratory, Department of Engineering Mechanics, Tsinghua University, 100084 Beijing, China; [r]Department of Biomedical Engineering, Northwestern University, Evanston, IL 60208; [s]Department of Neurological Surgery, Northwestern University, Evanston, IL 60208; [t]Department of Electrical Engineering and Computer Science, Northwestern University, Evanston, IL 60208; [u]Simpson Querrey Institute, Northwestern University, Evanston, IL 60208, USA; [v]Feinberg School of Medicine, Northwestern University, Evanston, IL 60208

[1]H.Z. and K.L. contributed equally to this work.

[2]To whom correspondence should be addressed. E-mail: jrogers@northwestern.edu, yihuizhang@tsinghua.edu.cn, or y-huang@northwestern.edu

www.pnas.org/cgi/doi/10.1073/pnas.1901193116

This PDF file includes:

Supplementary Table S1.
Supplementary Figures S1 to S17.

Structure	Height predicated by FEA (mm)	Height measured from experiments (mm)
Left, top	1.25	1.29
Left, middle	1.89	1.92
Left, bottom	4.39	4.50
Right, top	1.04	1.04
Right, middle	2.99	2.82
Right, bottom	1.18	1.32

Table S1. Comparisons of the final heights of the 3D structures (shown in Figure S5) in shape II predicated by FEA and measured from experiments.

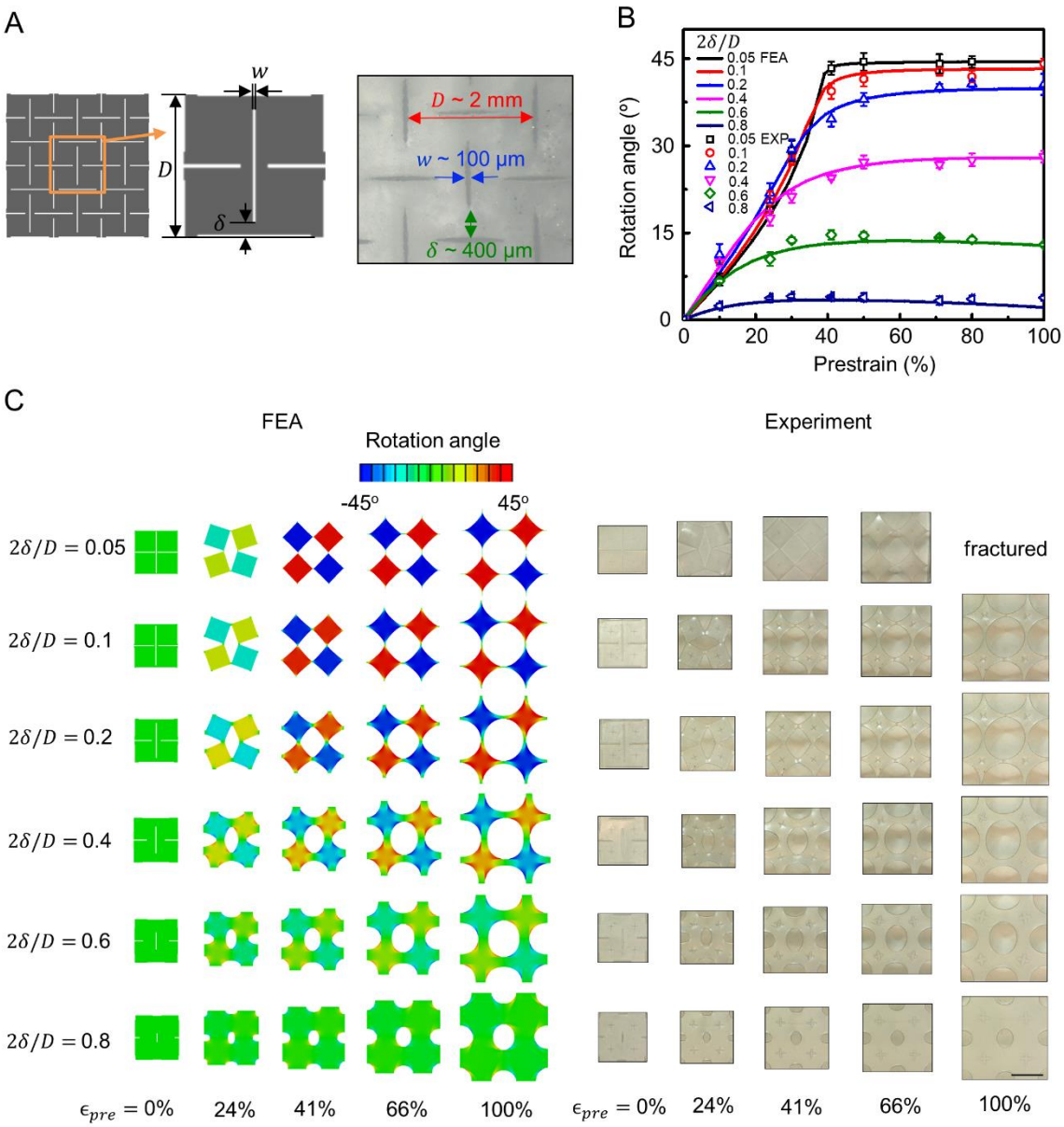

Figure S1. Design and deformation of kirigami elastomer substrates under biaxial stretching. (*A*) Schematic diagram and experimental image (optical) illustrating the geometric parameters employed in the pattern of cuts. (*B*) Comparison of rotation angles at the centers of the unit cells from FEA and experiments as a function of different $2\delta/D$ ratios and biaxial prestrain. (*C*) Color representations of the distributions of rotation angles and experimental images (optical) of a kirigami silicone elastomer substrate with different $2\delta/D$ ratios biaxially stretched from 0% to 100%. The unit cell size D is 8 mm and the cutting width w is 100 μm. Scale bar, 5 mm.

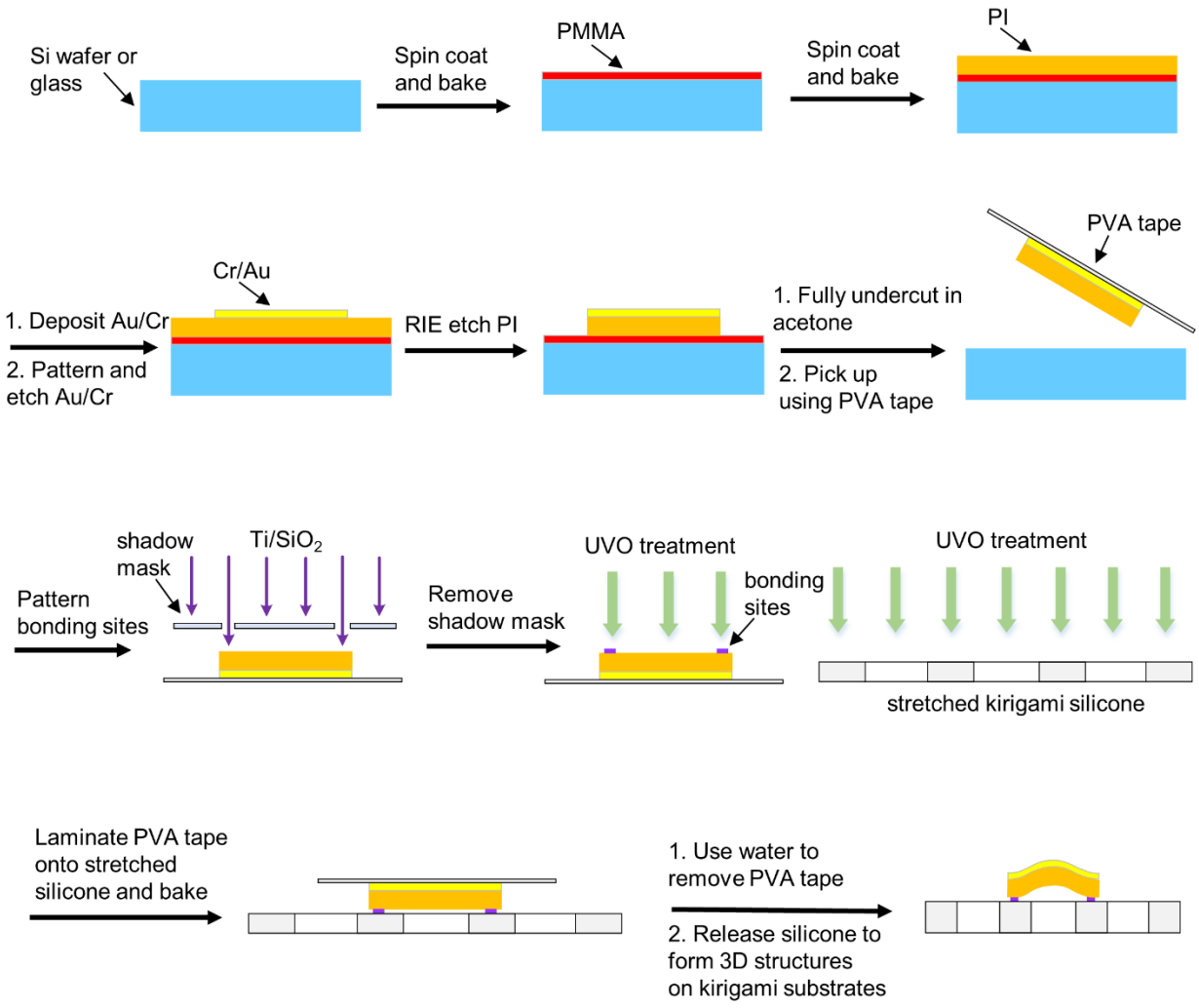

Figure S2. Schematic illustration of steps for fabricating 3D morphable structures on kirigami substrates.

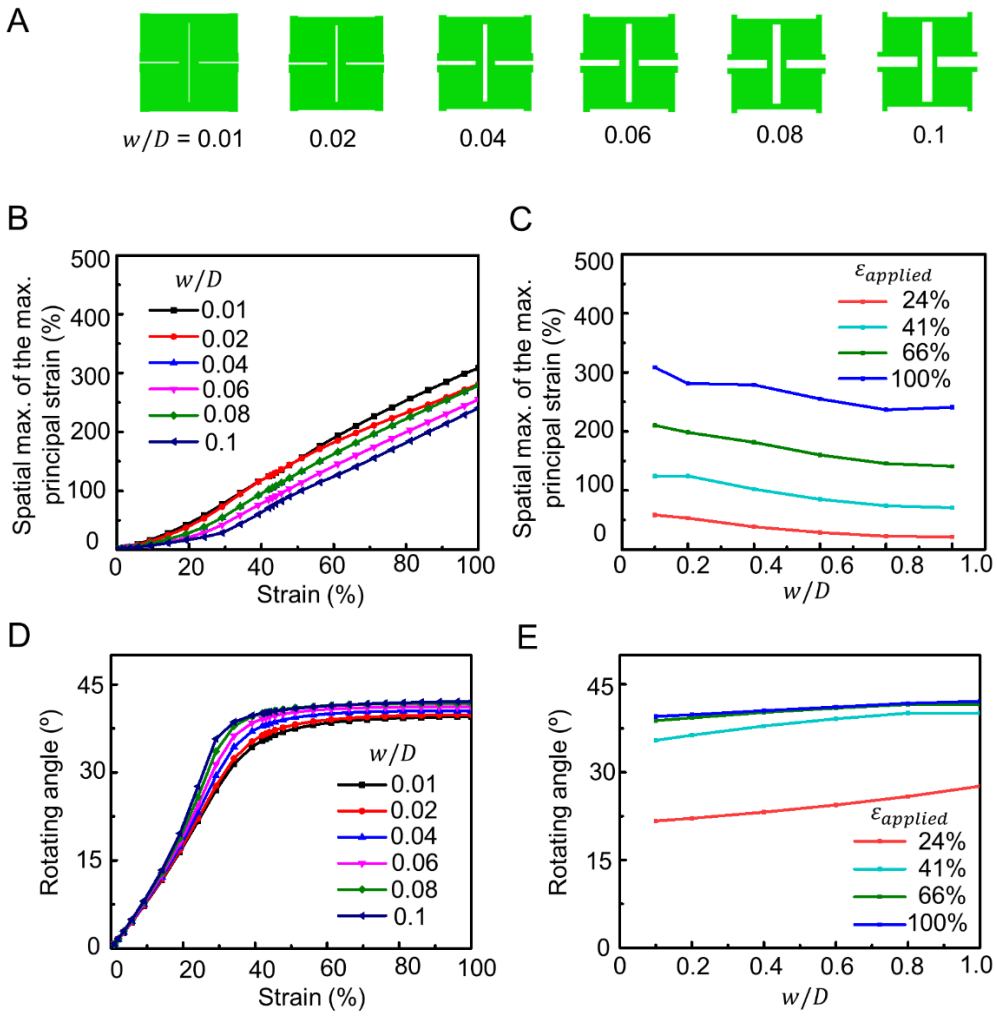

Figure S3. Dependence of the spatial maximum of the maximum principal strains and the unit rotation angles on the stretched kirigami substrate, as a function of the ratio of cut width to unit cell size (w/D) and applied biaxial prestrain from FEA. (*A*) Schematic diagram illustrating the geometries with various w/D ratios (from 0.01 to 1). (*B*) Plot of the spatial maximum of the maximum principal strain as a function of the biaxial prestrain with different w/D values (from 0.01 to 1). (*C*) Plot of the spatial maximum of the maximum principal strain as a function of w/D with different biaxial prestrain (24%, 41%, 66%, and 100%). (*D*) Plot of the rotation angle at the centers of the unit cells as a function of the biaxial prestrain with different w/D values (from 0.01 to 1). (*E*) Plot of the rotation angle at the centers of the unit cells as a function of w/D with different biaxial prestrain (24%, 41%, 66%, and 100%).

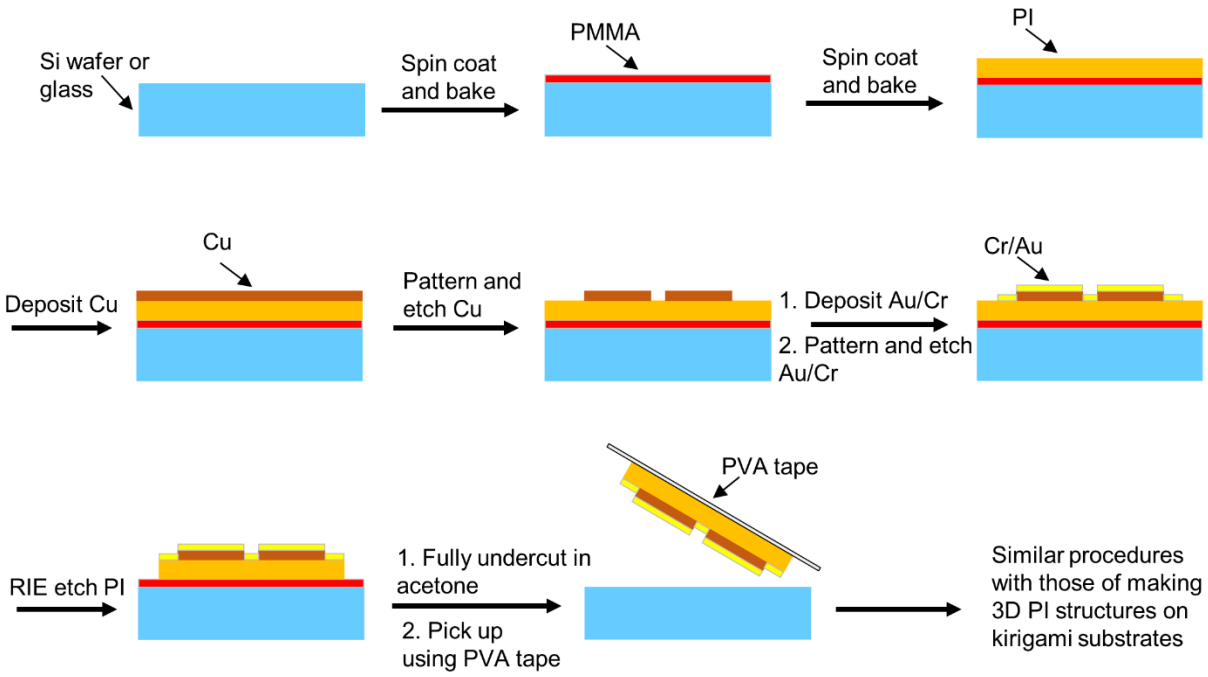

Figure S4. Schematic illustration of steps for fabricating 3D morphable, origami-inspired structures on kirigami substrates.

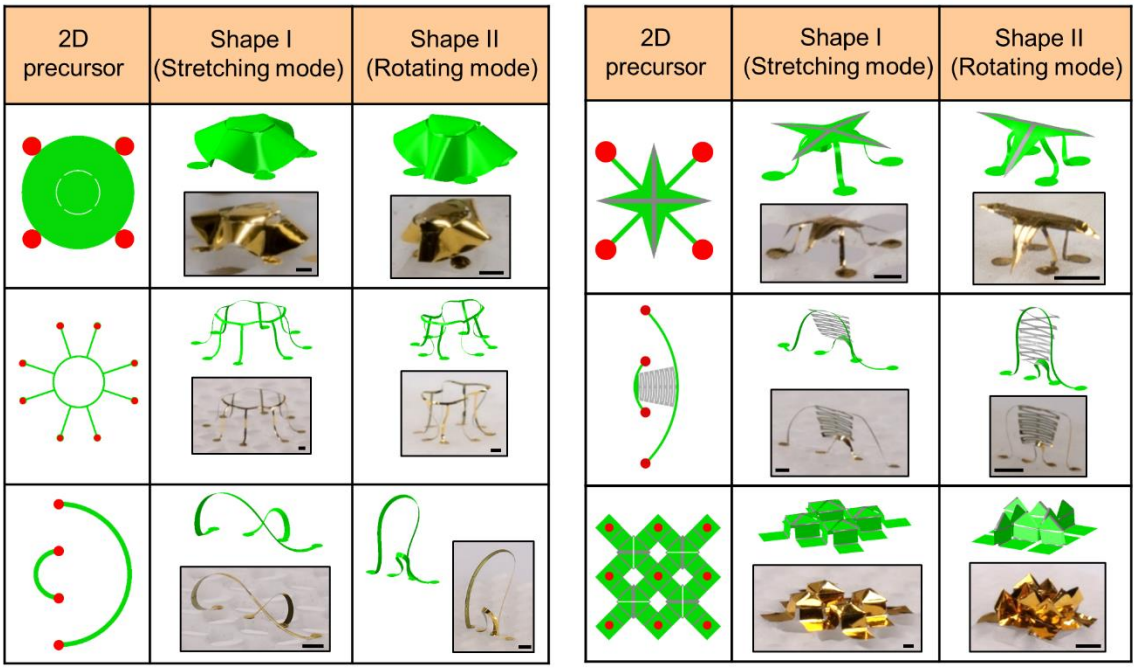

Figure S5. Incorporation of twisting into a broad set of 3D morphable mesostructures: 2D geometries, FEA predictions and experimental images (optical) of morphable 3D ribbon structures, membrane structures, and hybrid ribbon/membrane structures assembled on kirigami substrates. Shape I and shape II correspond to the 3D shapes after releasing of the stretching mode (prestrain from 100% to 40%) and releasing of the rotating mode (prestrain from 40% to 0%). Scale bars, 1 mm.

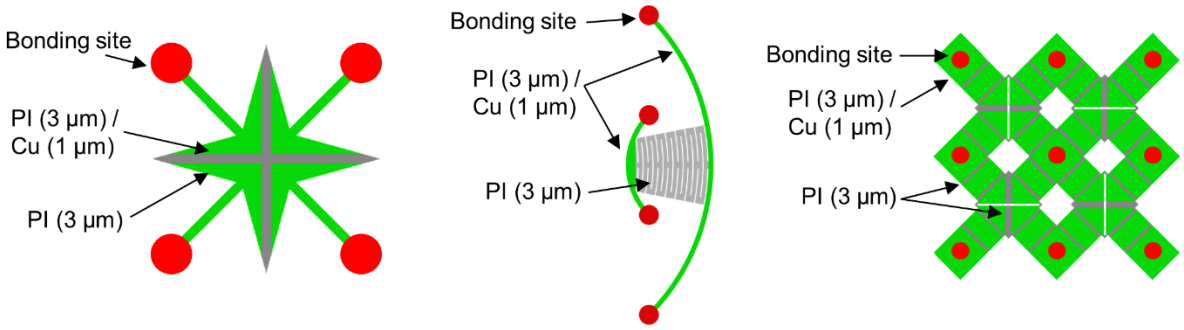

Figure S6. Schematic illustration of the 2D precursor designs for three exemplary origami-inspired structures.

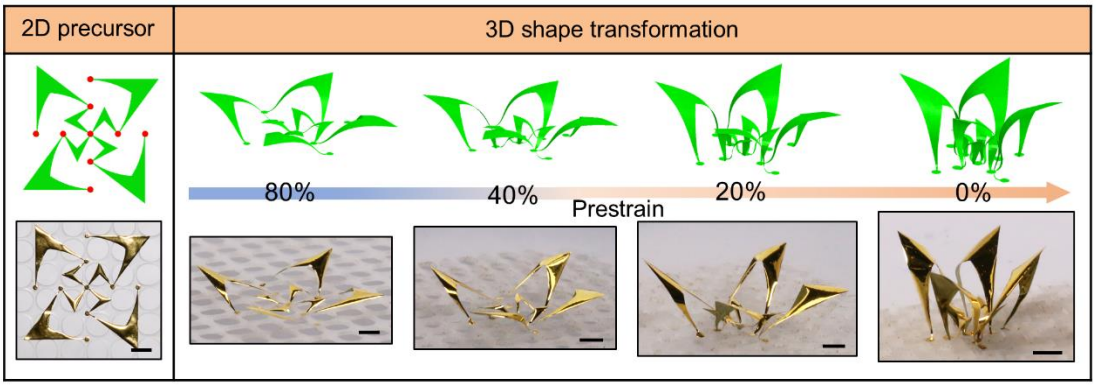

Figure S7. Demonstration of the continuous shape transformation of a sophisticated, flower-like 3D mesostructure enabled by buckling and twisting. Scale bars, 2 mm.

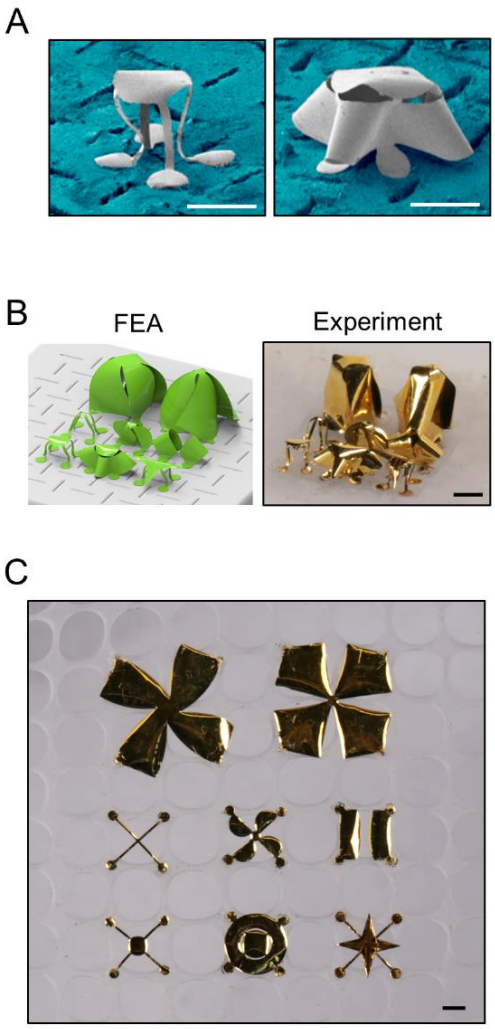

Figure S8. 3D morphable architectures at microscale and in an array formed by buckling and twisting. (*A*) Scanning electron microscope images of microscale 3D structures on kirigami substrates. (*B*) Experimental images (optical) and FEA results of an array of eight different 3D mesostructures, demonstrating the single-step, parallel feature of the assembly approach. (*C*) Optical image of the 2D precursors bonded to a prestretched kirigami substrate (100% prestrain) for the assembly of 3D structures shown in (*B*). Scale bars, 200 μm for structures in *A*, 1 mm for structures in *B* and *C*.

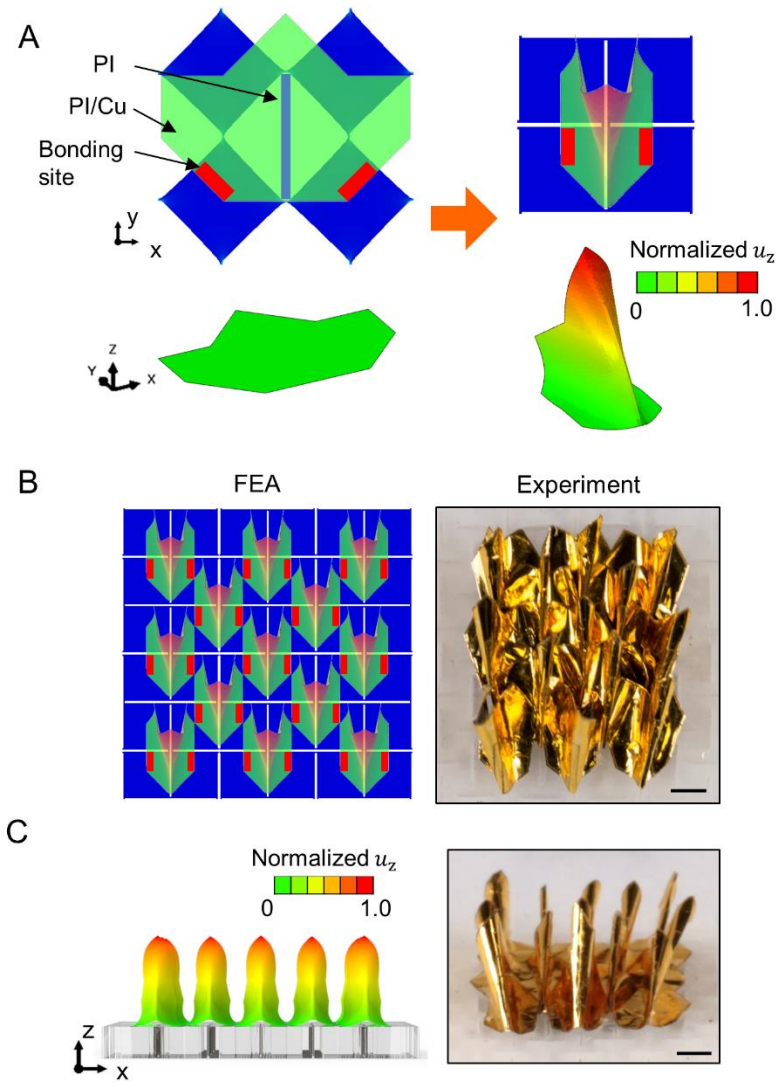

Figure S9. 2D geometries, FEA predictions and experimental images of an array of creased structures. (*A*) 2D precursor designs and FEA predictions (showing normalized displacements in z direction) of a unit creased structure before and after buckling and twisting. (*B*) Top-down view and (*C*) side view of FEA predictions and experimental images (optical) of an array of creased structures after buckling and twisting. Scale bars, 1 mm.

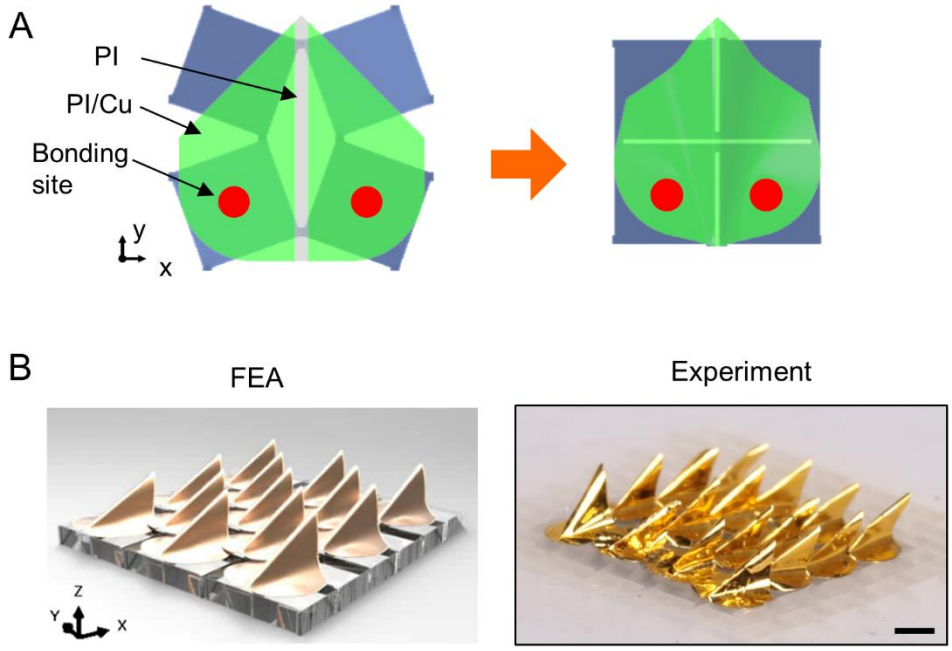

Figure S10. 2D geometries, FEA predictions and experimental images of a 4x4 array of creased structures. (*A*) Top-down view of 2D precursor designs and FEA predictions of a unit creased structure before and after buckling and twisting. (*B*) Isometric view of FEA predictions and experimental images (optical) of an array of creased structures after buckling and twisting. Scale bar, 1 mm.

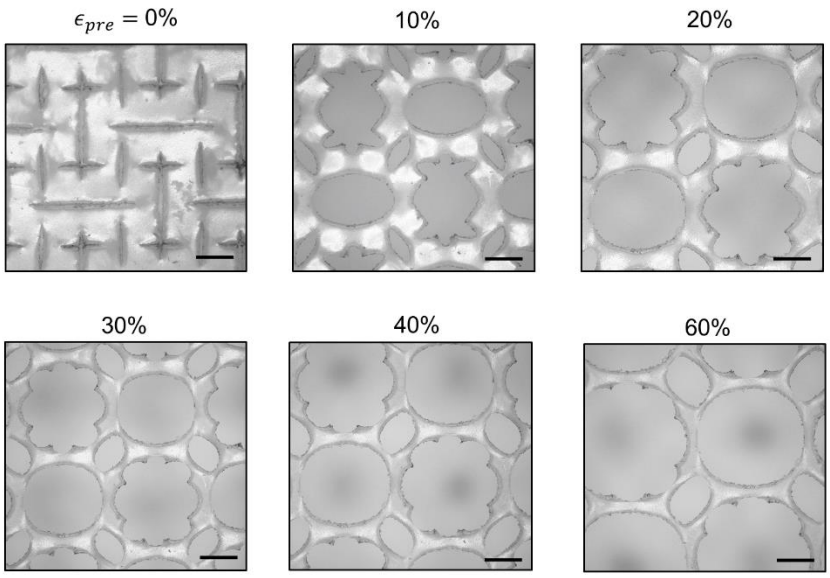

Figure S11. Optical images of a kirigami silicone elastomer substrate with two-level square cut pattern biaxially stretched from 0% to 60%. Scale bars, 1 mm.

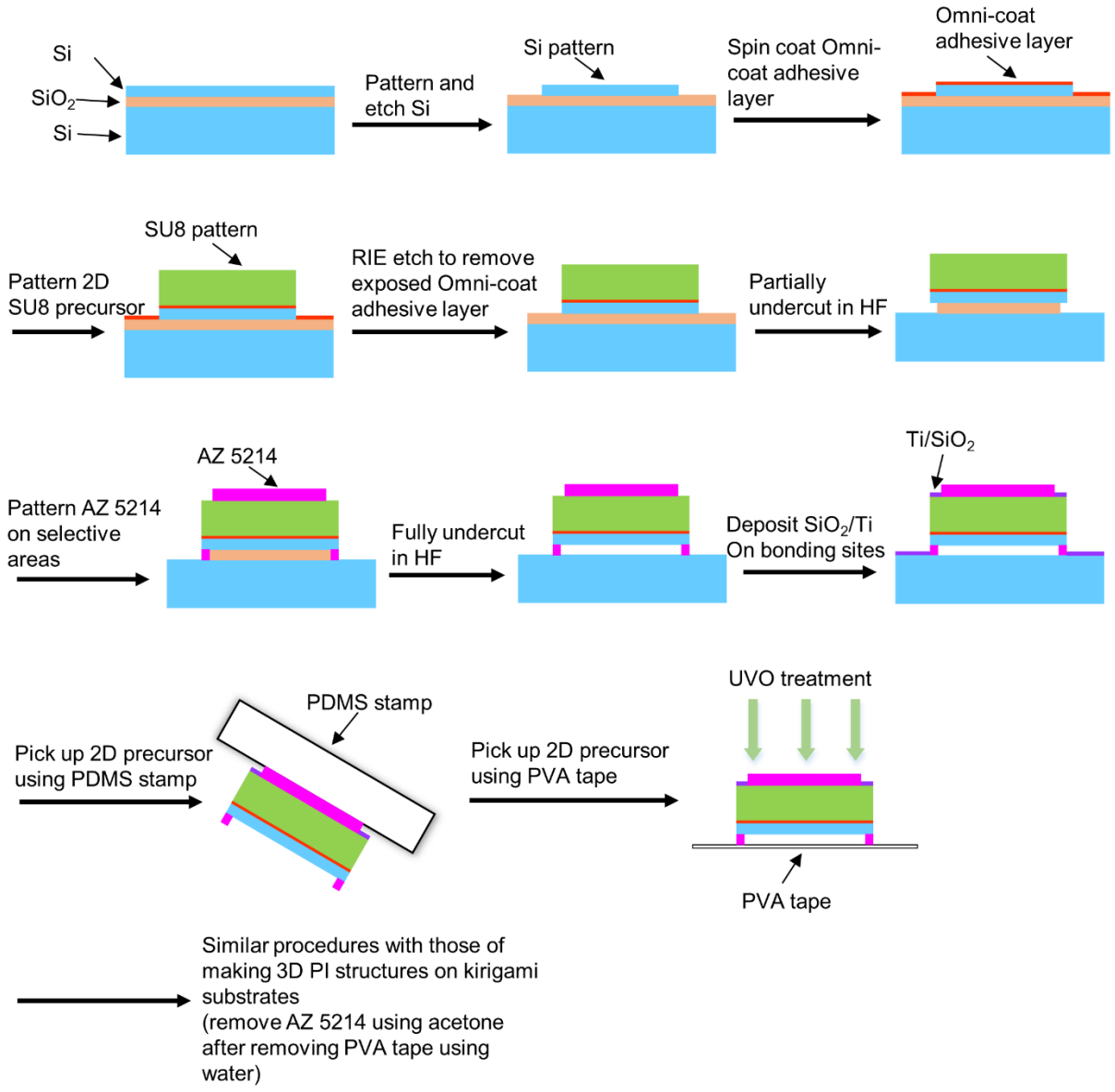

Figure S12. Schematic illustration of steps for fabricating 3D morphable, silicon-SU8 structures on kirigami substrates.

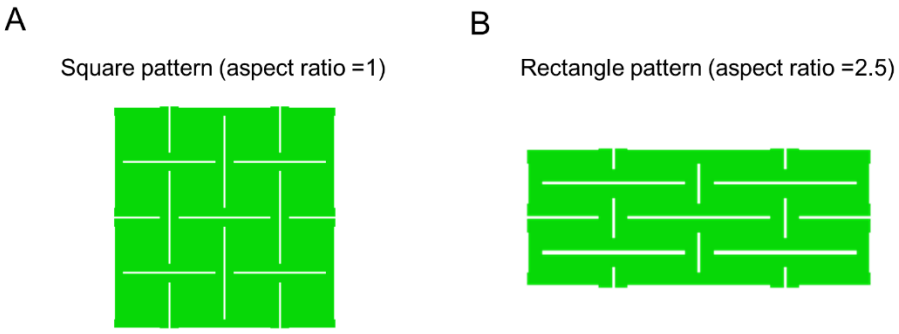

Figure S13. Schematic illustraions of (*A*) square cut pattern with a unit aspect ratio of 1 and (*B*) rectangular cut pattern with a unit aspect ratio of 2.5.

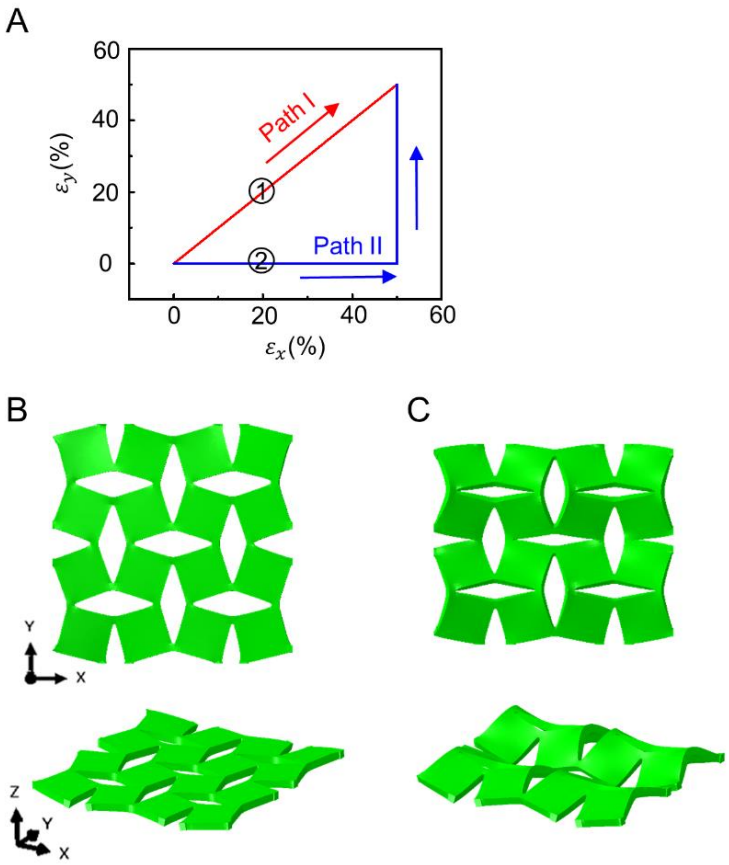

Figure S14. Wrinkle formation in elastomer substrates with square cut patterns during biaxial stretching. (*A*) Temporal sequence of changes in applied strains for two different loading paths. (*B*) Simultaneous biaxial stretching along path I in (*A*) does not create wrinkles while (*C*) sequential stretching along path II in (*A*) results in wrinkle formation. (*B*) and (*C*) correspond to the top-down and isometric views of state 1 and 2 shown in (*A*).

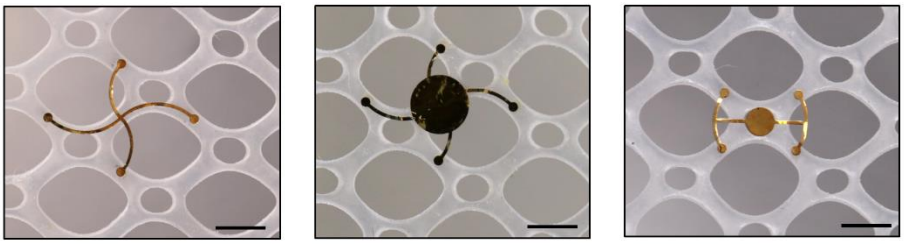

Figure S15. Optical image of three 2D precursors bonded to a prestretched kirigami substrate (50% prestrain in x axis, 125% prestrain in y axis) for demonstrating the incorporation of twisting into a loading-path controlled mechanical assembly mechanism. Scale bars, 2 mm.

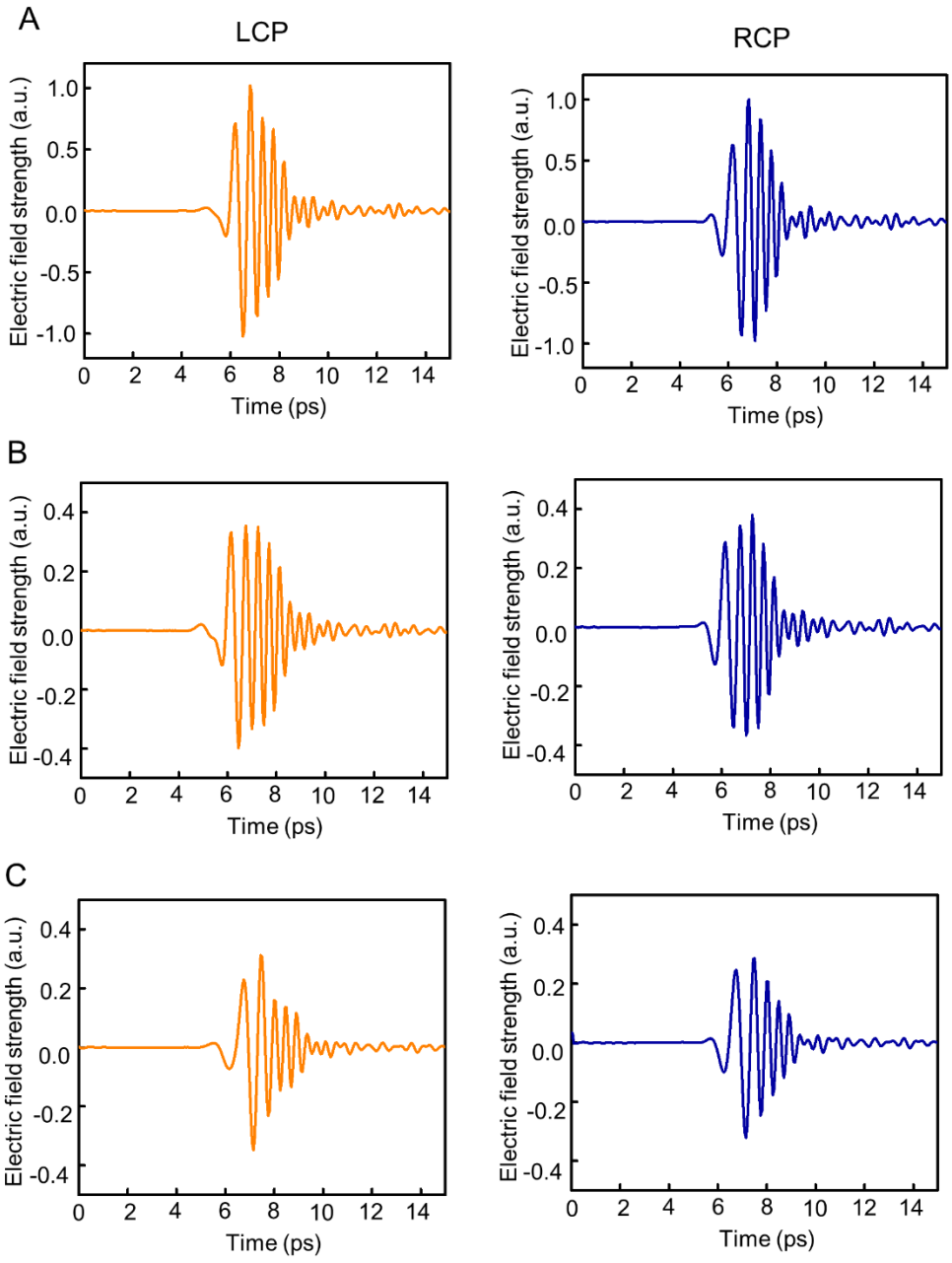

Figure S16. Measured THz electric field strength (arbitrary unit) as a function of time (unit: ps) under LCP and RCP for (*A*) blank, (*B*) shape I of the 3D trilayer microstructure (design I in Fig. 5*A*), and (*C*) shape II of the 3D trilayer microstructure.

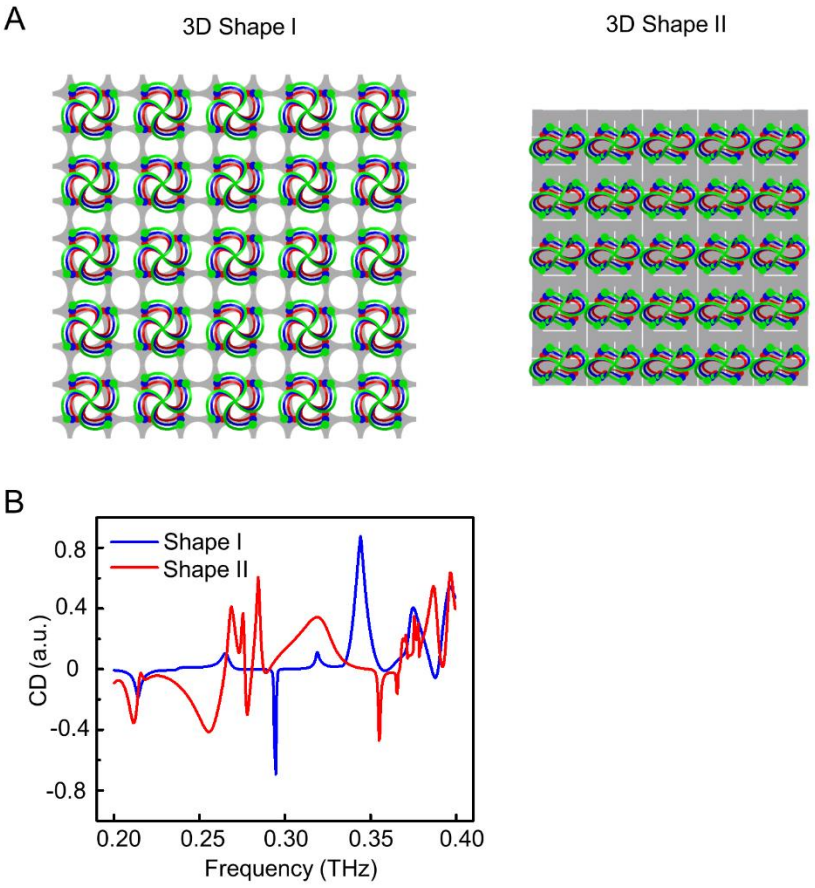

Figure S17. Simulations of an array of 3D morphable trilayer microstructures as mechanically tunable optical chiral metamaterials. (*A*) FEA results of a 5x5 array of 3D morphable trilayer microstructures (design I in Fig. 5*A*). (*B*) Electromagnetic simulation of the circular dichroism (*CD*) of an array of morphable 3D trilayer microstructures with two 3D shapes (design I in Fig. 5*A*) in the 0.2-0.4 THz frequency range.